Titre: Title: Gas-aggregated core–shell ZrN@SiN nanoparticles with enhanced thermal stability for plasmonic applications at high temperatures

Auteurs: Authors: Mariia Protsak, Veronika Cervenkova, Daniil Nikitin, Suren Ali-Ogly, Zdeněk Krtouš, Kateryna Biliak, Pavel Pleskunov, Marco Tosca, Ronaldo Katuta, Hynek Biederman, Bill Baloukas, Ludvik Martinu, Lucia Bajtosova, Miroslav Cieslar, Milan Dopita, & Andrei Choukourov

Date: 2025

Type: Article de revue / Article

Référence: Citation: Protsak, M., Cervenkova, V., Nikitin, D., Ali-Ogly, S., Krtouš, Z., Biliak, K., Pleskunov, P., Tosca, M., Katuta, R., Biederman, H., Baloukas, B., Martinu, L., Bajtosova, L., Cieslar, M., Dopita, M., & Choukourov, A. (2025). Gas-aggregated core–shell ZrN@SiN nanoparticles with enhanced thermal stability for plasmonic applications at high temperatures. ACS Applied Nano Materials, 8(6), 3092-3103. https://doi.org/10.1021/acsanm.4c06843

Titre de la revue: Journal Title: ACS Applied Nano Materials (vol. 8, no. 6)

Maison d'édition: Publisher: American Chemical Society

URL officiel: Official URL: https://doi.org/10.1021/acsanm.4c06843

ACS APPLIED NANO MATERIALS

www.acsanm.org

Article

Gas-Aggregated Core−Shell ZrN@SiN Nanoparticles with Enhanced Thermal Stability for Plasmonic Applications at High Temperatures

Mariia Protsak,* Veronika Červenková, Daniil Nikitin, Suren Ali-Ogly, Zdenek Krtous, Kateryna Biliak, Pavel Pleskunov, Marco Tosca, Ronaldo Katuta, Hynek Biederman, Bill Baloukas, Ludvik Martinu, Lucia Bajtosova, Miroslav Cieslar, Milan Dopita, and Andrei Choukourov*

Cite This: *ACS Appl. Nano Mater.* 2025, 8, 3092−3103

Read Online

ACCESS | Metrics & More | Article Recommendations | Supporting Information

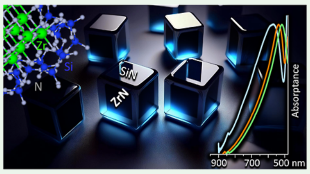

ABSTRACT: Group IV metal nitrides are often considered a viable replacement for gold in numerous plasmonic applications that require high temperatures. However, despite exhibiting a high melting point, these materials are prone to oxidation in an oxygen-rich environment, leading to an undesirable change or loss of the plasmonic response. This work developed an environmentally friendly method based on reactive magnetron sputtering of Zr for the synthesis of ZrN nanoparticles (NPs) with their in-flight coating by an rf-sputtered SiN shell. The resultant core−shell NPs are characterized by cubic morphology, with a 15 nm ZrN core enveloped by a 5−15 nm SiN shell. The ZrN@SiN NPs demonstrate localized surface plasmon resonance (LSPR), which can be adjusted from 580 to 850 nm by tuning the porosity and, consequently, the effective refractive index of SiN. The SiN shell attenuates the plasmonic sensitivity of ZrN NPs, but protects them from postdeposition oxidation in air, preserving LSPR at temperatures above 400 °C. Thus, this research proposes a one-step synthesis of ZrN@SiN NPs with controllable optical properties, enhanced thermal stability, and promising features for plasmonic applications at high temperatures.

KEYWORDS: *zirconium nitride, silicon nitride, gas aggregation cluster source, reactive magnetron sputtering, nanoparticles, thermal stability*

1. INTRODUCTION

Refractory materials with localized surface plasmon resonance (LSPR) are extremely interesting for several potential applications that rely on the plasmonic effects at high temperature: heat-assisted magnetic recording,[1] direct absorption solar collectors,[2,3] photothermal therapy of tumors,[4,5] high-temperature sensing,[6] photocatalysis,[7] and others. In particular, group IV transition metal nitrides (TMN) were often considered economically feasible replacements for noble metals, revealing comparable or even superior optical properties. These TMN are characterized by partially overlapping conduction and valence bands with a nonzero density of states at the Fermi level. They also show LSPR in visible/near-IR regions[6,8] and benefit through high melting points and hardness. Excellent chemical stability at high temperatures is also notoriously reported, although it has recently been questioned, especially for nanodispersed TMN that come into contact with oxidizing media such as air or water.[9−12] Uncontrollable incorporation of oxygen atoms in surface layers may not be critical for these materials on a macroscopic scale; but for nanomaterials, where the contribution from surface effects is significant, it may lead to an uncontrollable change in optoelectronic properties and, eventually, to complete loss of plasmonic response. In this regard, the protection of TMN nanomaterials with antioxidation barrier was considered either by depositing thin protective films on planar TMN substrates,[13−16] by processing of TMN NPs in solution[17] or through the in-flight coating of TMN NPs in the gas phase.[18,19] In many cases, silicon nitride (SiN) or oxynitride was the material of choice because it is characterized by high thermal stability, good insulating properties, and high hardness that make these films valuable as masks or protective layers.[20] The high refractive index and an almost zero extinction coefficient in the visible range are additional benefits that allow tuning the optical properties. For example, exciting results were obtained on photonic spin Hall effect and optical temperature sensing using metasurfaces of TiN and ZrN combined with SiN.[16,21]

The fabrication of TMN/SiN nanostructures often requires the deposition of thin films on hot substrates, sometimes accompanied by the use of aggressive chemicals such as silanes and NH_3. To better meet the requirements of sustainable development, the search for new synthetic pathways that avoid high temperatures and hazardous compounds is highly important. Our recent studies have introduced a method for the synthesis of TMN NPs via reactive magnetron sputtering in Ar/N_2 mixtures with the use of a gas aggregation cluster

Received: December 6, 2024
Revised: January 28, 2025
Accepted: January 29, 2025
Published: February 3, 2025

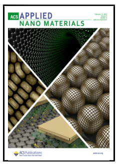

https://doi.org/10.1021/acsanm.4c06843

source (GAS).[22−25] Sputter-based GASes have long been known as ultraclean devices that utilize low-temperature plasma to produce metal NPs in an inert atmosphere of noble gases.[26−29] The lack of solvents, the low amount of waste, and compatibility with microelectronic technologies are long-known benefits of low-temperature plasma processing that make these approaches highly attractive in the modern technological paradigm.[30−32] If naturally abundant N_2 is added to the gas phase of the GAS, sputtering can be performed in a reactive mode and, under carefully chosen conditions, highly crystalline, stoichiometric TMN NPs can be produced and deposited on substrates at room temperature. The plasmonic sensitivity of these NPs was found to exceed that of Au;[25] however, they suffered from the same shortcoming of partial oxidation after contact with air. Therefore, the first goal of this work is to develop a method to passivate TMN NPs with protective SiN layers using an environmentally friendly approach. To this end, we opt for the in-flight deposition of SiN over TMN NPs to perform the modification without contact with air, and we chose radio frequency (rf) magnetron sputtering of Si_3N_4 because this solvent-free method produces almost no waste. The second goal of this work is to study whether the plasmonic features of TMN NPs can be tuned by adjusting the properties of the SiN shell and to establish the high-temperature limits for the plasmonic sensing abilities of these NPs.

2. EXPERIMENTAL AND CALCULATIONS

2.1. Deposition Setup. An experimental setup included a gas aggregation cluster source for the synthesis of ZrN NPs, a modification chamber for the in-flight deposition of SiN coatings over the ZrN NPs, and a deposition chamber for the collection of the ZrN@SiN NPs[a] on substrates (Figure 1). The GAS was constructed as a water-cooled cylindrical chamber 10 cm in diameter equipped on one side with a 3-in. planar magnetron and a Zr target (0.125-in. thick, grade 702 purity, Kurt J. Lesker). On another side, it comprised a conical endpiece with a cylindric orifice which separated the GAS from the modification chamber. It was possible to install the orifices with different diameters, whereas the length of the cylindrical hole was always kept at 2 cm. The modification chamber was equipped with two 3-in. planar magnetrons with Si_3N_4 targets (3.18 mm thick, 99.9% purity Kurt J. Lesker), facing each other and installed transversely to chamber axis. This chamber was separated from the deposition chamber by another conical endpiece with a cylindrical orifice of 25 mm in length. Its diameter was chosen based on results of computational fluid dynamics, CFD, calculations (see below). The deposition chamber was equipped with a movable quartz crystal microbalance (QCM) system used to measure the deposition rate of NPs. NPs were collected on Si substrates, TEM grids (Lacey Carbon Coated Copper Mesh, SPI Supplies), and quartz substrates (UV-grade, fused silica, 10 × 10 mm, 0.5 mm thick, SPI Supplies) introduced into the deposition chamber through a load lock. Additionally, the middle chamber was equipped with another load lock with the possibility to place substrates in front of the Si_3N_4 magnetrons.

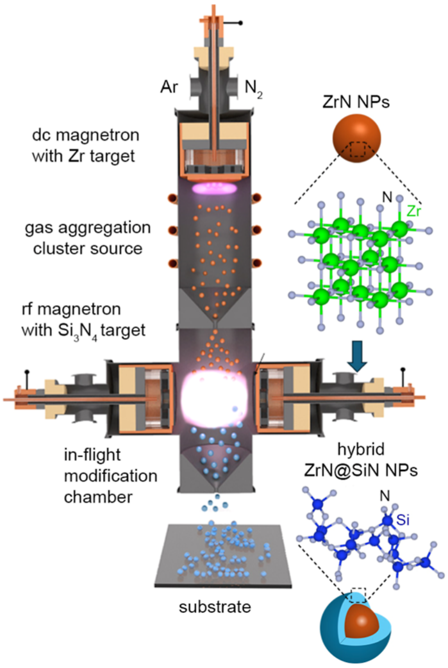

Figure 1. Scheme of the experimental setup for reactive sputter-driven synthesis of ZrN NPs and their in-flight coating with SiN.

Before the experiments, the setup was pumped down to a pressure of 10^{-3} Pa by rotary and diffusion pumps. The synthesis of ZrN NPs was performed by reactive sputtering of Zr in the mixture of Ar and N_2 according to a protocol developed and published earlier.[23] The current on the Zr magnetron was maintained at 500 mA using a dc power supply (PD500X, Kurt J. Lesker). The flow rates of Ar (purity 99,996%, Linde AG) and N_2 (purity 99.999%, Linde AG) were controlled by two independent mass flow controllers (MFC, MKS Instruments). The flow rate of Ar was fixed at 6.0 sccm, while the flow rate of N_2 was sequentially increased in steps of 0.02 sccm per 30 s until the value of 0.28 sccm was reached, at which the bias at the magnetron showed an abrupt increase, indicating the onset of the reactive sputtering mode. At these conditions, the pressure in the GAS was 50.0 Pa. Sputtering of Si_3N_4 was performed in the modification chamber using rf power supplies (13.56 MHz, R301, Kurt J. Lesker) coupled to the Si_3N_4 magnetrons via automatic matching network controllers (MC2, Kurt J. Lesker). The pressure in the modification chamber was 8.7 Pa. Prior to any experiment, precleaning of the Si_3N_4 targets was required as discussed in (Supporting Information Table S1). The pressure in the deposition chamber was 0.1 Pa in all experiments.

2.2. Characterization of NPs. The morphology and structure of the NPs were studied using a (scanning) transmission electron microscope ((S)TEM, 2200FS, JEOL Ltd., Japan) equipped with a FEG cathode operated at 200 kV of acceleration voltage in bright and high angle annular dark filed (BF and HAADF) imaging. Measurements were performed on NPs deposited on copper grids coated with lacey carbon. The elemental composition was investigated by energy dispersive analysis in STEM (STEM-EDS, Centurio Large Angle SDD-EDX detector, JEOL Ltd., Japan). Moreover, for structural analysis, scanning electron microscopy (SEM, JSM-7200F, JEOL Ltd.) was also used. The measurements were made at 20 kV acceleration voltage and 3×10^{-10} A probe current capturing cross-section sample orientation.

The crystal structure was determined by X-ray diffraction (XRD) measurements performed on a Rigaku SmartLab diffractometer with a rotating copper anode (Cu Kα radiation λ = 0.15418 nm) in the parallel beam geometry. Data analysis was done using the MStruct software.[33]

The chemical composition was studied with an X-ray photoelectron spectrometer (XPS, Phoibos 100, Specs) equipped with an Al Kα X-ray source (1486.6 eV, 200 W, Specs). For this analysis, ZrN, ZrN@SiN NPs, and SiN films were deposited on Si substrates and XPS spectra were acquired at a takeoff angle of 90°. The wide and high-resolution spectra were recorded at a pass energy of 40 eV (dwell time 100 ms, step 0.5 eV) and 10 eV (dwell time of 100 ms, step size of 0.05 eV, with 10 repetitions), respectively. Quantitative analysis was performed with the use of the CasaXPS software (v. 2.3.19PR1.0, Casa Software Ltd.), with a charge correction to adventitious carbon (the C 1s peak at 285.0 eV). The best fits for the Zr 3d peak were obtained using a Gaussian−Lorentzian (70/30) algorithm after a Shirley background subtraction. All XPS measurements were performed at room temperature (RT) and after air annealing at 200, 300, and 700 °C (heating at a rate of 5 °C/60 s).

Transmission (*T*) and reflection (*R*) spectra of ZrN and ZrN@SiN NPs deposited on one-inch square quartz substrates were obtained at RT within the wavelength range of 250−2500 nm using a spectrophotometer (Lambda 1050, PerkinElmer, Inc.) equipped with an integrating sphere. Absorption (*A*) was calculated as 100 − *T* − *R*, where both *T* and *R* comprise the specular and diffuse components. Furthermore, *T* spectra were acquired during annealing in air in a furnace (Barnstead Thermolyne) equipped with a UV−Vis spectrophotometer (MCS621, Carl Zeiss Spectroscopy) attached to the furnace via an optical fiber. Transmission spectra were measured within the wavelength range of 345−1051 nm with an acquisition time of 4 s per spectrum. Each sample was continuously heated from 25 to 700 °C under a heating rate of 20 °C/min.

The SiN films deposited on Si substrates were also analyzed by spectroscopic ellipsometry (M2000DI, J. A. Woolam) for determination of their thicknesses and optical constants. Measurements were conducted in the wavelength range from 400 to 1700 nm at three angles: 55, 65, and 75°. The ellipsometry data were fitted using CompleteEASE software (J. A. Woollam) employing two approaches. First, the single-phase Cauchy model was involved with the next change to the Effective Medium Approximation model (EMA, Bruggeman) with two components: Si_3N_3O and voids.

2.3. Calculations. The gas flow and the transport of NPs were analyzed by performing CFD calculations similar to our approach published elsewhere,[34] the details given in Supporting Information. Briefly, Siemens STAR CCM+ software (double precision version) was used. Steady-state analysis was performed employing a segregated flow solver with the 2d order convection. A SIMPLE pressure−velocity (semi-implicit method for pressure linked equations) coupling algorithm was used to solve the Navier−Stokes equations. In regions with transitional flow (0.01 < Knudsen number < 0.1), the Maxwell slip correction was applied. The temperature of the gas in the CFD simulation was set to 21 °C. The simulation accounted for temperature changes due to expansion in the orifice region, as shown in Figure S1 of Supporting Information. Details of the pressure drop across the orifice can be seen in Figure S2 of Supporting Information, where a magnified region of orifice 2 is shown.

After the fluid field data were obtained, NPs were added to the system as solid-state spherical particles. Their motion was solved transiently (the unsteady-state), taking the necessary fluid flow information from the previous steady-state simulations. The Lagrangian approach was used to describe the evolution of individual particles as they traverse the domain.

Optical extinction of NPs was simulated using the Mie Scattering software.[35] Simulations were performed for spherical ZrN NPs with and without a shell of material with different refractive indices. Vacuum was chosen as the surrounding medium.

3. RESULTS AND DISCUSSION

3.1. Transport of NPs and Deposition of Thin Films.

The integration of the modification chamber in between the GAS and the deposition chamber introduces an additional element of complexity to the transport of NPs driven by the gas flow. Under constant gas supply and pumping speed, the pressure and the linear gas velocity in the modification chamber can be controlled by the size of orifice 2. A challenging task is thus to find the optimal orifice size that would satisfy two opposing demands: (1) the pressure in the modification chamber should be high enough to prolong the time that NPs spent in front of the auxiliary magnetrons undergoing their in-flight coverage with SiN, and (2) the pressure should be sufficiently low to ensure a collisionless sheath at the SiN target (making SiN sputtering efficient) and a larger mean free path of the sputtered material (increasing its supply to the axial area of the GAS). Computational fluid dynamics (CFD) calculations were performed to determine the gas flow dynamics and velocity of NPs for three sizes of orifice 2 and, as a consequence, for three different pressure values in the modification chamber. Furthermore, two different NP sizes of 10 and 50 nm were chosen to account for the fact that the ZrN NPs produced in the GAS are not monodispersed.[23] Figure 2a shows an example of the gas velocity map for a pressure of 12.4 Pa (orifice 2 is 7 mm in diameter), while Figure 2b gives the evolution of velocities of 10 and 50 nm NPs along the axis of the modification chamber calculated for three different pressures.

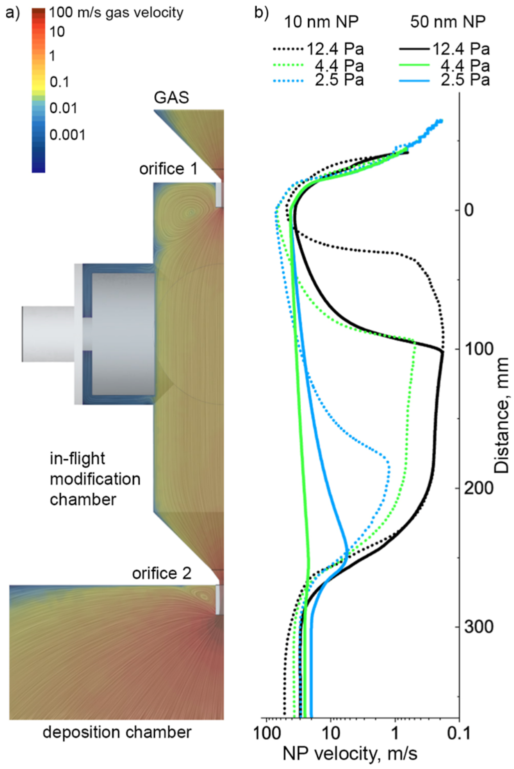

Figure 2. (a) Half cross-section of the modification chamber with the gas streamlines calculated by CFD and colorized in accordance with gas velocity (orifice 2 is 7 mm in diameter, pressure 12.4 Pa); (b) velocities of 10 and 50 nm NPs along the axis of the chamber calculated for different pressures; zero distance corresponds to the position of orifice 1.

The gas streamlines demonstrate laminar flow in the entire volume of the modification chamber, except for the region close to orifice 1, where vortices can be observed. NPs enter the modification chamber with subsonic velocities and are then retarded due to drag forces, with the retardation depending on the pressure and the size of the NPs. Higher pressure poses a higher drag force on NPs and results in faster retardation. On the other hand, larger NPs possess higher mass and have higher inertia, which results in slower retardation (more rigorous calculations and discussion can be found in Table S2 of Supporting Information). Therefore, for the purpose of slowing down the NPs, it is preferable to operate with small NPs under higher pressures. For example, one can compare the velocity of 10 nm NPs at 12.4 Pa (black dotted line in Figure 2b) with that of 50 nm NPs at 2.5 Pa (blue line in Figure 2b). The former decrease their velocity by 2 orders of magnitude before reaching the region of the auxiliary magnetrons, whereas the latter remain largely unaffected, reaching the second orifice without a significant drop in their velocity. Consequently, the residence time of NPs in the region between the SiN magnetrons can be substantially different, depending on the pressure and NP size (Table 1). For the mentioned ultimate cases, the residence time ranges from 0.428 to 0.0024 s, covering a two-order magnitude in time scale.

Table 1. Calculated Time That NPs Spent When Passing the Zone of the Magnetron Discharge (76 mm) along the Chamber Axis for Different Pressures (Different Sizes of Orifice 2); the Shaded Data Correspond to the Conditions Used in the Experiments

diameter of orifice 2 , mm	pressure in the modification chamber, Pa	residence time, s	
		10 nm NP	50 nm NP
7	12.4	0.428	0.219
11	4.4	0.084	0.032
15	2.5	0.0028	0.0024

Considering the dilemma between the residence time and the efficiency of the SiN sputtering process, we chose the second orifice with a diameter of 7 mm for experiments, noting that the experimentally measured pressure of 8.7 Pa was lower than 12.4 Pa predicted by the CFD calculations. A series of experiments were carried out with the GAS turned off and Si substrates placed on the axis of the modification chamber in front of the SiN magnetrons as shown in inset of Figure 3a. Only one SiN magnetron was operated, and the dependence of the deposition rate on the rf power was evaluated (Figure 3a). The dependence is observed to be linear, with the deposition rate reaching 17 nm/min at 100 W. Markedly, if the deposition rate on the planar substrate is mechanistically translated onto in-flight deposition on NPs considering their residence time in front of the magnetrons, simple estimations give a thickness of the SiN overcoat of about 0.12 on 10 nm NPs, which is very low. Experiments refute these mechanistic findings, and we will address this intriguing mismatch in the following section.

Spectroscopic ellipsometry detected that the effective refractive index of the SiN films increases with the rf power (Figure 3b). Interestingly, the XPS analysis showed that the films are oxidized; however, their chemical composition does not change with power and can be represented by the generic formula of Si_3N_3O (the total elemental content is given in Table S3 of Supporting Information). Therefore, it was assumed that the films have porous structure, a phenomenon inherent in plasma-grown SiN coatings. For example, it was shown that the porosity of SiN films can depend on various factors, including applied bias or temperature, and that the different levels of porosity result in a variation of the refractive index.[36−38]

In our case, the sputtering is performed at a relatively high pressure (low mean free path), which results in fast thermalization of the sputtered SiN species before they reach the substrate. Consequently, surface diffusion lacks thermal activation from hyperthermal neutrals, leading to the growth of the porous structure.

To account for porosity, a simple single-component Cauchy ellipsometry model was replaced with a two-component model (EMA, Bruggeman) consisting of SiN and voids. Given that the solid component is oxidized Si_3N_3O, its refractive index was chosen to be n_{630} = 1.70, considering the proportional mixture of Si_3N_4 and SiO_2, so it fitted reasonably between the values of stoichiometric Si_3N_4 (n_{630} = 2.04) and SiO_2 (n_{630} = 1.46). Figure 3c shows the power dependence of the fraction of voids calculated using this approach. Although the absolute values may be biased by an error in choosing the refractive index of Si_3N_3O, the general trend is obvious: the fraction of

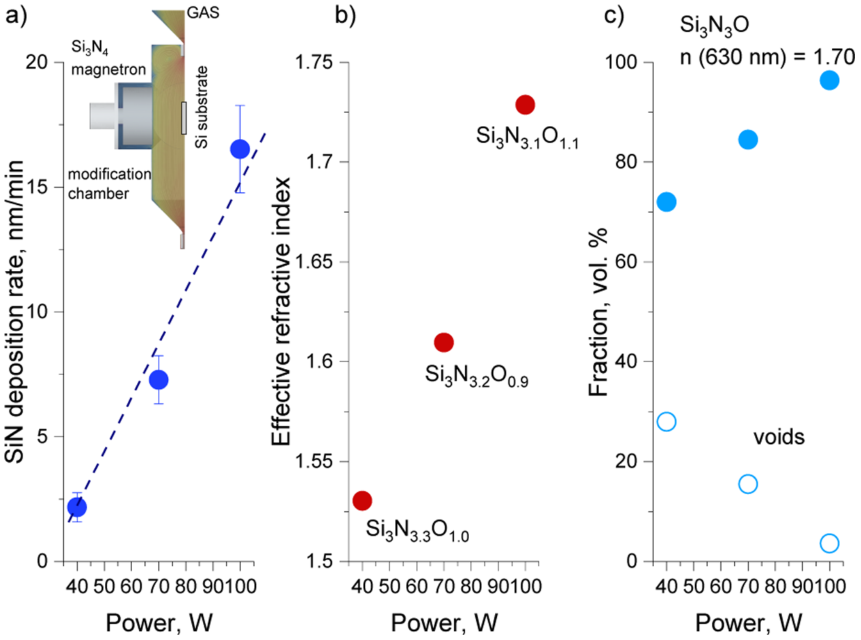

Figure 3. (a) Dependence of the deposition rate of SiN films deposited on planar Si substrates placed on the axis of the modification chamber in front of the Si_3N_4 magnetron as shown in inset (8.7 Pa pressure, no ZrN NPs involved); (b) effective refractive index (λ = 630 nm) of these films as measured by ellipsometry and calculated using a single-phase Cauchy model; (c) volume fraction of voids in these films calculated using the two-phase Bruggeman model with $n_{630\text{ nm}}$ = 1.70 fixed for Si_3N_3O and $n_{630\text{ nm}}$ = 1.00 fixed for voids. Chemical formulas shown are derived from XPS analysis.

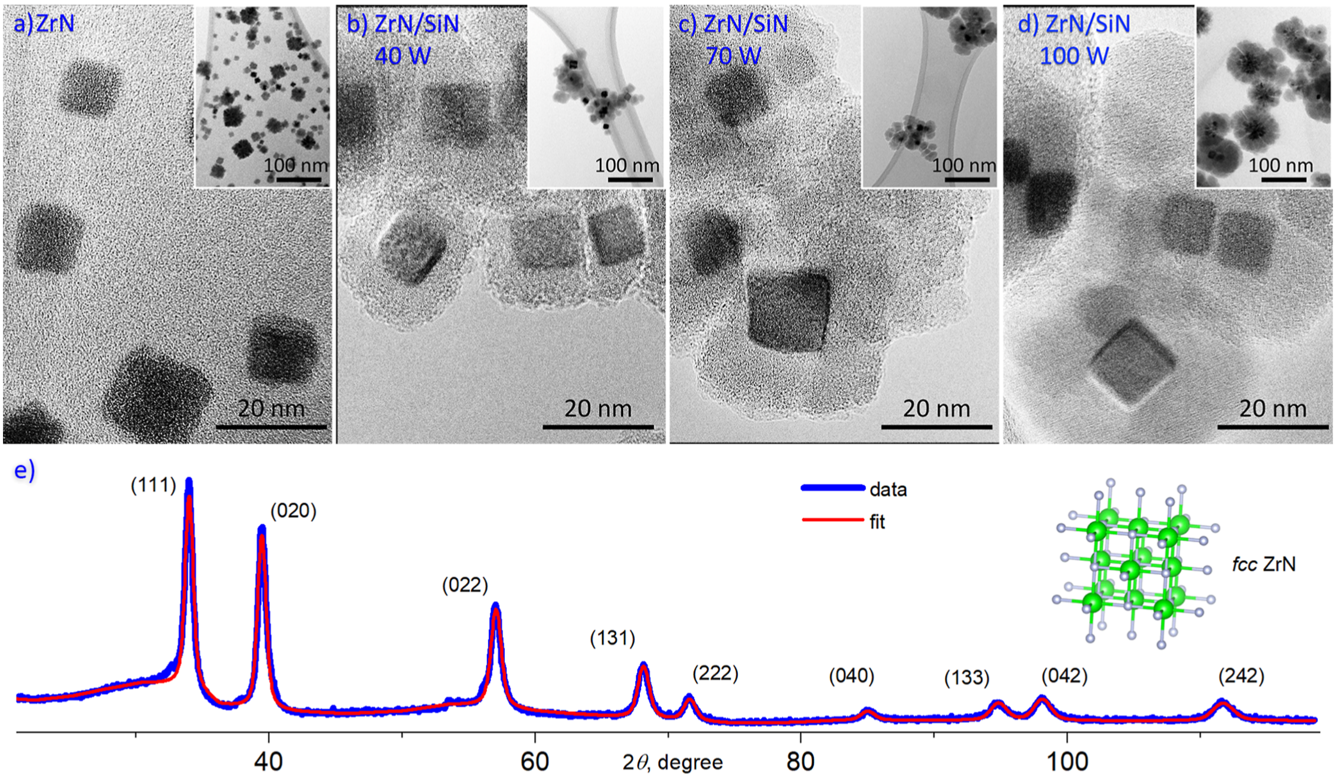

Figure 4. (a−d) TEM images of ZrN NPs and ZrN@SiN NPs prepared at different rf powers applied to the Si_3N_4 magnetron; (e) XRD pattern of ZrN NPs: red curve is fit to data shown in blue; the inset shows the fcc unit cell of ZrN.

voids decreases significantly with increasing rf power, reflecting the denser character of the SiN films prepared at higher powers. In this case, the stronger bombardment of the NP surface by ions from the plasma sheath competes with the limited surface diffusion of neutral SiN species arriving onto NPs almost thermalized. Our complementary gravimetric measurements showed that the density of SiN films increases from 2.38 g/cm^3 for 40 W to 2.65 g/cm^3 for 100 W (for details see Supporting Information). These values are lower than the tabulated 3.17 g/cm^3 for the bulk Si_3N_4,[39] which also points to the porosity of the coatings.

3.2. Morphology of NPs. In accordance with our previous reports,[22,23] reactive sputtering of Zr in the GAS produces ZrN NPs. Figure 4a−d shows the TEM images of ZrN NPs that passed through the modification chamber with or without one of the SiN magnetrons turned on. Bare ZrN NPs, i.e. those without the SiN shell, are of cubic shape and characterized by a log−normal size distribution with the mean size of 15 ± 7 nm (Figure 4a). The cubic morphology stems from the inner crystalline structure; indeed, XRD analysis showed a well-resolved crystalline pattern of the fcc phase, space group 225 belonging to ZrN (Figure 4e).

Figure 4b−d shows the TEM images of ZrN NPs prepared with one SiN magnetron operating at 40, 70, or 100 W. The most striking result to emerge from these images is that distinct shells can be observed around the ZrN NPs. Interestingly, the shells are deposited conformally, framing the ZrN NPs and replicating their cubic shape, which speaks for substantial angular momenta on the NPs traveling in the auxiliary discharge region. The shells are thicker at higher rf powers, as can be seen from the NP size distributions shown in Figure S3 of Supporting Information, and also from an indirectly supportive XPS analysis, which will be discussed below.

In general, the shells are up to 15 nm thick, which is particularly surprising considering the extremely small values predicted by the previous mechanistic calculations. One reasonable explanation for this inconsistency is that, in reality, NPs spend a much longer time in the modification zone than predicted based on the gas flow simulations. Our earlier work discovered the capturing of NPs in magnetron-based GAS, which was attributed to their charging and retention in the plasma due to the interaction with the electric field.[28,29] In fact, the retention of NPs on a time scale of seconds was experimentally demonstrated. Furthermore, rf discharges were shown to retain NPs even for hours if they are specifically configured with respect to cluster source.[11] Therefore, we hypothesize that the observed thicker-than-predicted shell is due to the longer residence time of ZrN NPs in the modification chamber caused by their capturing in the auxiliary magnetron discharge. Following our mechanistic ansatz and implying speculatively that SiN grows on ZrN NPs with a deposition rate similar to that on Si substrate, we come to a curious discovery that NPs should spend minutes in the auxiliary plasma before they leave the modification zone. Based on these findings, further experiments were limited to a single SiN magnetron used for the in-flight modification.

3.3. Chemical Composition and Optical Properties. Given the experimental design, it can be assumed that the shells present on ZrN NPs and observed in the TEM images consist of sputtered SiN. To support this assumption, STEM-EDS elemental mapping was performed on the chosen area of the grid with ZrN@SiN (100 W) NPs. Figure 5 shows the bright and dark field STEM images of these NPs with the corresponding elemental maps for Zr (blue), N (green), and Si (red), the overlay of these false colors is also shown. Obviously, the signal from Zr is localized in the NP core,

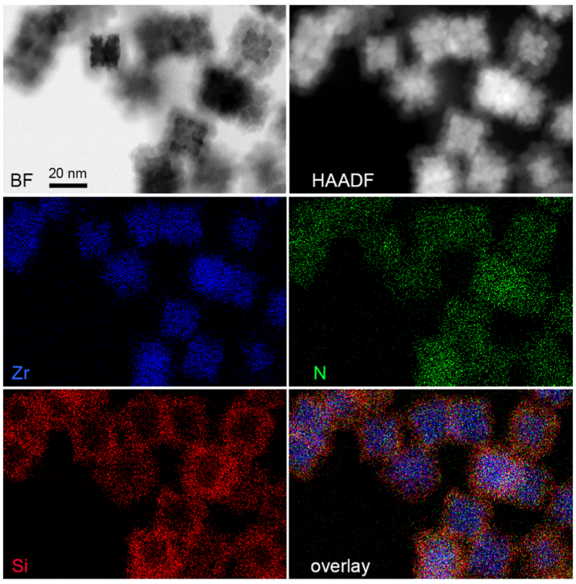

Figure 5. STEM-EDS analysis of ZrN@SiN NPs (100 W rf power applied on the Si_3N_4 magnetron): BF and HAADF STEM images; false colored Zr, N, and Si STEM elemental maps and their overlay.

the signal from Si comes from the shell, while the signal from N is evenly distributed throughout the NP volume, confirming that the NPs consist of a ZrN core and SiN shell.

The in-flight deposition of SiN over ZrN NPs leads to an interesting modulation in the optical properties of coatings prepared from these NPs. Optical transmission and reflection spectra were recorded on ZrN and ZrN@SiN NPs prepared at different applied rf powers on the Si_3N_4 magnetron (Figure 6a,b), and absorptance spectra were calculated as described in the experimental section (Figure 6c). (Transmission, reflection, and absorptance spectra of bare quartz substrates are given in Figure S4 of Supporting Information). It is worth noting that the reflection spectra (comprising the specular and diffuse components) do not reach beyond several percents of the total intensity, except for the near-UV region, where reflection slightly increases. This hints at high porosity and low effective refractive index of the coatings. Therefore, the transmission and absorptance spectra are almost inverse replicas of each other. Bare ZrN NPs strongly absorb at wavelengths below 500 nm due to p → d interband transitions and also in the red/near-IR region due to the localized surface plasmon resonance (LSPR). With the addition of a SiN shell, the UV–Vis spectra retain their overall shape, although their LSPR maximum blue shifts from 850 to 580 nm with the increasing power on the Si_3N_4 magnetron. Thus, our approach allows for tuning the position of the LSPR absorption peak from the visible to the near-IR range.

The downside of the thick dielectric shell present on the surface of ZrN NPs is that it may significantly attenuate the plasmonic sensitivity of LSPR transducers built from these materials. Our previous calculations showed that NPs of group IV transition metal nitrides exhibit a plasmon effective decay length of several nanometers,[25] which determines the length scale for the chemical and biological sensing. The presence of a thicker dielectric shell should inevitably attenuate the evanescent plasmon field to a level impractical for plasmonic sensing. On the other hand, porosity of the shell may play a role in favor of plasmonic sensitivity. To estimate the plasmonic sensitivity of the ZrN@SiN NPs, we ultrasonicated the 100 W sample in two liquids with known refractive indices: H_2O (n_{630} = 1.33) and polyethylene glycol (PEG400, n_{630} = 1.47). The optical transmission of these solutions was measured by UV–Vis and the position of the LSPR peak in dependence on the refractive index of the surrounding medium was obtained (Figure 6d). The red shift of the LSPR is observed with increasing refractive index, although the slope of 24 nm/RIU (RIU is refractive index unit) is not very high. The nonzero plasmonic sensitivity supports the idea of pores present in the SiN shell: these may be infiltrated by molecules of host liquids, bringing the analyte closer to the ZrN/SiN

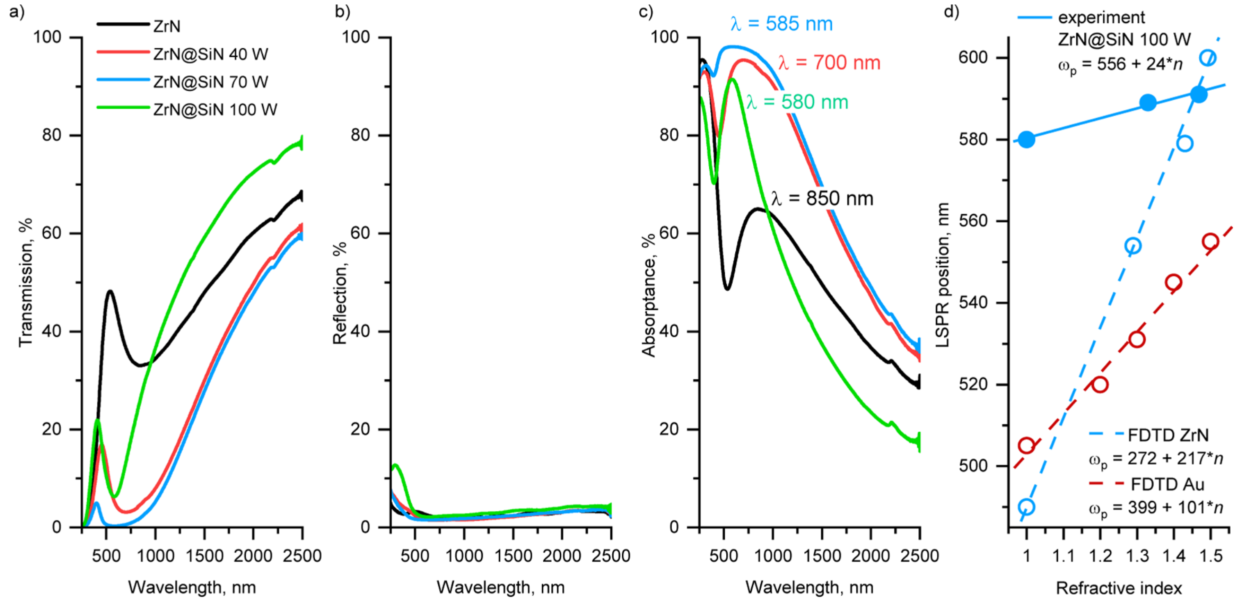

Figure 6. Optical properties of ZrN NPs and ZrN@SiN NPs prepared at different rf powers on Si_3N_4 magnetron and deposited on quartz substrates: (a) transmission T; (b) reflection R; (c) absorptance A; (d) LSPR position of ZrN@SiN 100 W NPs in dependence on refractive index of the surrounding medium.

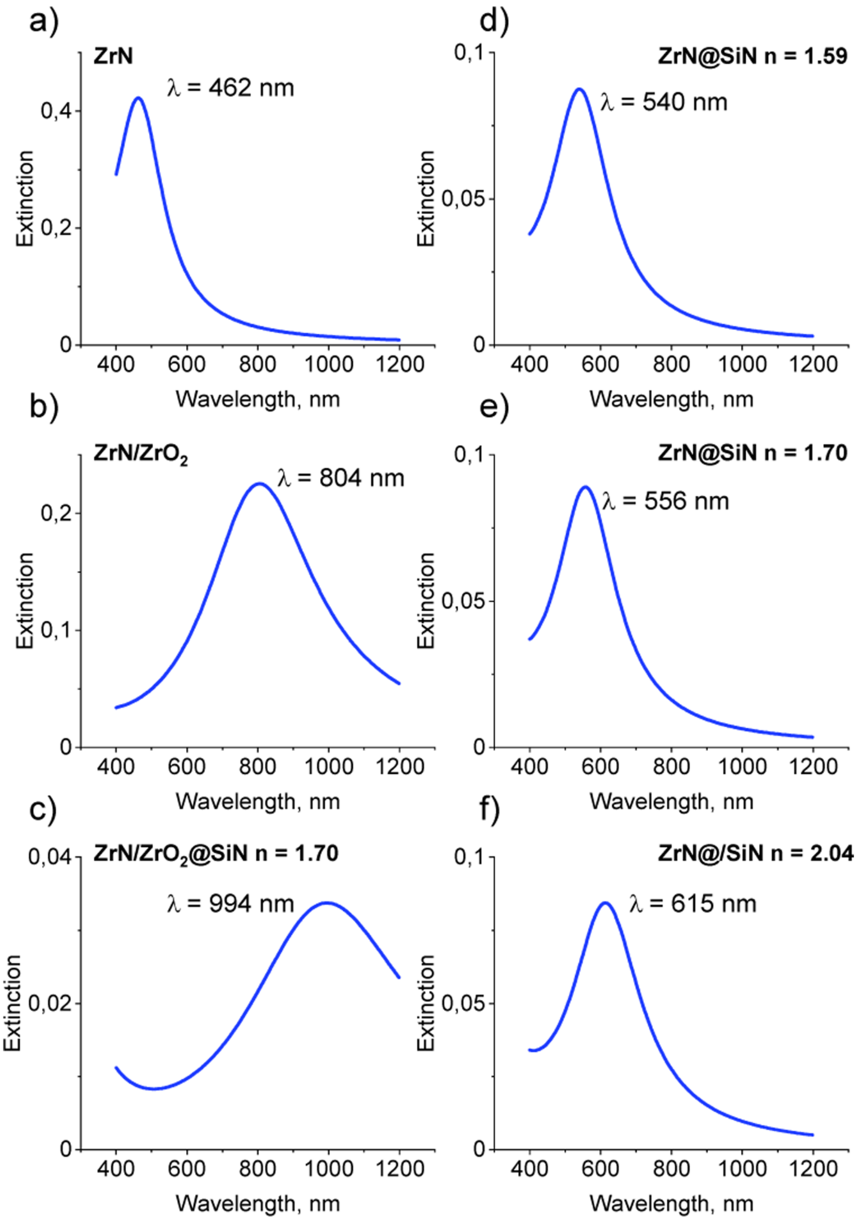

Figure 7. Calculated optical extinction spectra: (a) stoichiometric ZrN NPs; (b) oxidized ZrN NPs approximated by a 30/70 mixture of ZrN and ZrO_2; (c) oxidized ZrN NPs with SiN shell (n_{630} = 1.70); (d−f) stoichiometric ZrN NPs with SiN shells with n_{630} = 1.59, 1.70, and 2.04. The size of the ZrN NPs is 15 nm, and the thickness of the SiN shell is 15 nm.

interface. For comparison, Figure 6d provides the plasmonic sensitivities of ideal ZrN and Au NPs determined by FDTD calculations in our previous work.[23] Obviously, the ideal ZrN NPs reveal an order of magnitude higher sensitivity than ZrN@SiN (100 W) NPs, even surpassing the conventional Au NPs. Nevertheless, we believe that ZrN@SiN NPs can still be useful, especially for the plasmonic sensing at high temperatures, where conventional Au and unprotected ZrN may fail.

Our previous research showed that ZrN NPs are vulnerable to postdeposition oxidation even at room temperature.[23] To elucidate the influence of the SiN shell on the oxidation resistance of ZrN, the calculations of the optical extinction spectra were carried out. (Scattering spectra were also calculated, but they do not contribute substantially to the total extinction cross-section, as shown in Figure S5 of Supporting Information). First, the calculations were performed for ideally stoichiometric 15 nm-sized ZrN NPs and they confirmed the earlier findings: the calculated spectrum shows the LSPR in the blue range at 462 nm (Figure 7a), while the experimentally measured value is strongly red-shifted to 850 nm, pointing to the partial oxidation of ZrN NPs after their extraction from vacuum. To further demonstrate the oxidation effect, we replaced the dielectric function of stoichiometric ZrN with that of an arbitrarily chosen 30/70 mix of ZrN and ZrO_2, which resulted in a similar redshift of the LSPR to the near-IR (Figure 7b). The calculations were also performed on oxidized ZrN NPs covered by the 15 nm SiN shell with n_{630} = 1.70, corresponding to the value experimentally measured for 100 W SiN films. The addition of the shell shifts the LSPR further to the IR range (Figure 6c), which contradicts the position found experimentally at 580 nm (Figure 5). The disagreement between the calculations and experiments can be resolved if we assume that the SiN shell formed in-flight on ZrN NPs serves as a barrier layer, hindering

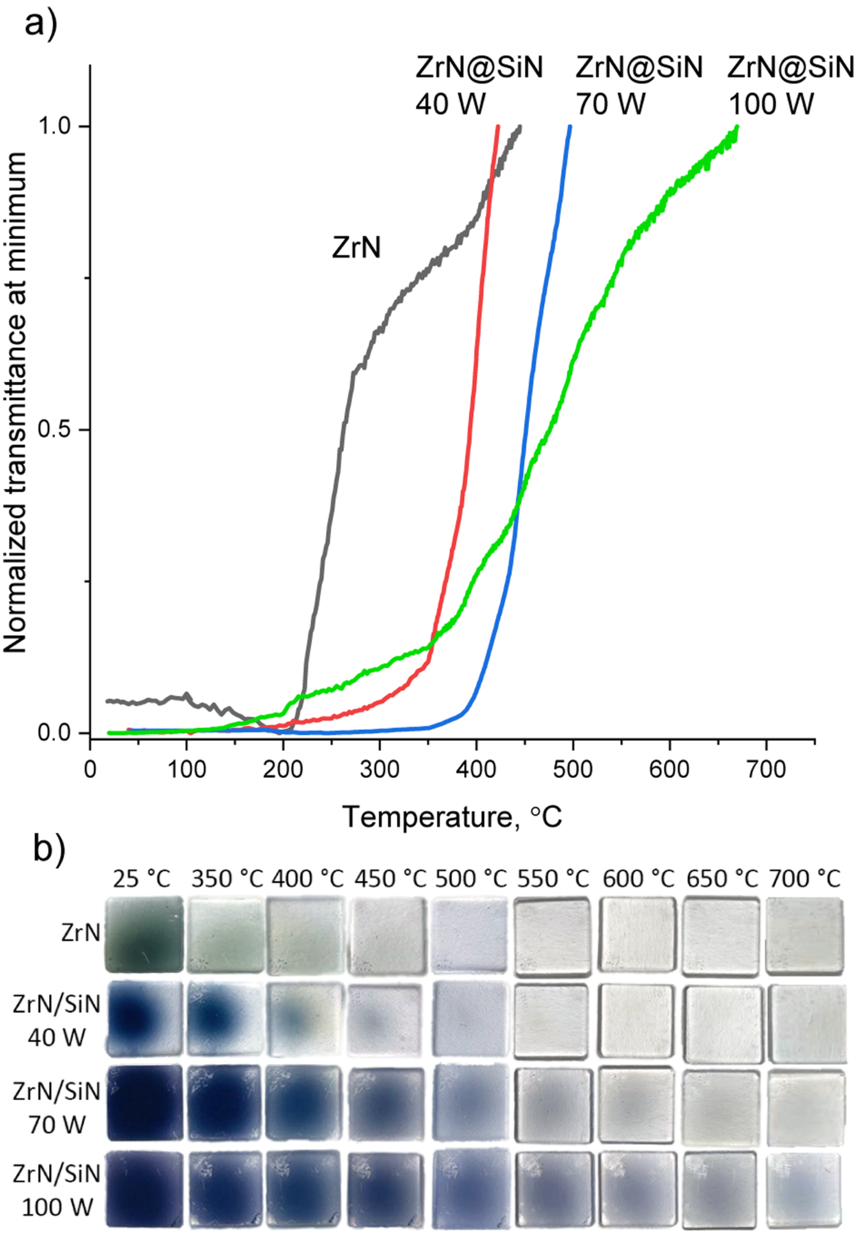

Figure 8. (a) Evolution of optical transmittance at the position of LSPR minimum for each curve of ZrN NPs and ZrN@SiN NPs with shell deposited at different applied powers on the SiN magnetron measured in situ during annealing in air and (b) photos of the samples taken ex-situ after the annealing at different temperatures.

the postdeposition oxidation of ZrN. Indeed, the calculations reveal that stoichiometric ZrN NPs covered with the SiN shell of different refractive indices resonate at shorter wavelengths: the LSPR position is located between 540 and 615 nm for n_{630} varying between 1.46 (SiO_2) and 2.04 (Si_3N_4) (Figure 6d−f). This range fits well with the experimentally obtained numbers. Thus, the position of the LSPR by the in-flight deposition of SiN can be tuned by taking advantage of two opposing factors: the postdeposition oxidation of bare ZrN NPs which shifts the LSPR to near-IR and the influence of the antioxidation SiN barrier which shifts it to the visible range.

3.4. Thermal Stability in Air.

Group IV transition metal nitrides are often considered refractory materials with excellent thermal stability. However, when present in a nanoscale form, their thermal resistance can be substantially compromised even under vacuum or inert gas environments.[40−42] For air, the situation becomes even worse, as was shown by recent reports.[25,43] Given that the SiN shell retards the postdeposition oxidation of ZrN NPs at RT, we decided to investigate whether this protection will also be effective at higher temperatures in the air. Optical transmittance spectra were measured on ZrN and ZrN@SiN NPs deposited on quartz substrates during their in situ heating in air up to a temperature of 700 °C (Figure S6 of Supporting Information). For all the samples, the transmittance remains unchanged until a certain temperature is reached, after which it starts to increase in the whole wavelength range. For better visualization, the normalized transmittance at the position of LSPR minimum for each curve was plotted as a function of temperature in Figure 8a. ZrN NPs are observed to be the least stable, showing an onset of optical transformations at 200 °C. The LSPR completely vanishes at 400 °C; hence, no data are available on the LSPR beyond this temperature. This thermal behavior is consistent with our recent results obtained on HfN NPs prepared by reactive magnetron sputtering.[25] As expected, ZrN@SiN NPs are more stable due to the presence of the protective shell. The transmittance starts increasing at 300 °C for ZrN@SiN (40 W) NPs and 400 °C for ZrN@SiN (70 W) NPs, while the LSPR disappears at 400−450 °C for these two samples. The sample of ZrN@SiN (100 W) NPs does not reveal an abrupt onset of the LSPR changes, unlike the other samples. The transition is more gradual, and it is hard to establish a specific crossover temperature. Interestingly, the LSPR is still visible for this sample even at the highest temperature of 700 °C, although the shape of the LSPR band characterized by the local minimum changes to the curve with the inflection.

Visual inspection of the samples after air annealing also confirms that stability increases in the sequence of ZrN → ZrN@SiN (40 W) → (70 W) → (100 W). It is interesting to note that the as-prepared coatings present saturated colors: the bare ZrN NPs are green, while the color changes to blue for ZrN@SiN (40 W) and further to purple for ZrN@SiN (70 and 100 W). Markedly, similar tints were observed on the inverse system of core−shell NPs, in which commercial SiO_2 NPs were decorated with ZrN NPs prepared by a solid-state metathesis reaction.[44] In that case, however, the investigated particles were substantially larger (150−300 nm SiO_2 NPs decorated with 10−30 nm ZrN NPs) and the resultant color was given predominantly by the Bragg diffraction on large SiO_2 NPs contributed also by absorption due to LSPR of ZrN NPs.

After annealing in air, our coatings lose color and become more transparent. The effect can be observed in the images of the four samples sequentially heated to a specific temperature, cooled down to RT, and photographed (Figure 8b). However, the transformation occurs in different temperature ranges for these four samples, with bare ZrN NPs and ZrN@SiN (100 W) showing the least and the most thermal stability, respectively, consistent with the spectra.

The observed optical changes are given in part by the chemical transformations discussed below and in part by the densification of the NP deposits. Figure S7 of the Supporting Information shows SEM images of the spatial rearrangement of the NPs accompanied by the reduction of the total volume occupied by the NPs in the deposit, approaching the limit of random close packing, while Figure S8 of the Supporting Information shows TEM details of structural changes both in the cores and shells. Thus, one may expect that the optical properties of these coatings would change even in the absence of any chemical transformations. In reality, however, the structural changes are also accompanied by transformations in the chemical composition.

Regardless of numerous reports on the excellent chemical stability of ZrN films, ZrN NPs are prone to surface oxidation even at RT. Figure 9a shows their Zr 3d XPS spectrum deconvoluted into three pairs of spin−orbit split $3d_{5/2}$ and $3d_{3/2}$ components, corresponding to ZrN (180.5 and 182.9 eV), ZrNO (181.8 and 184.2 eV), and ZrO_2 (182.3 and 184.7 eV). A strong contribution from the oxygen-containing components confirms the existence of an oxynitride shell on the surface of ZrN NPs, as was also shown in our previous work.[23]

The Zr 3d XPS spectra were acquired on the same sample after air annealing at different temperatures (Figure 9b). For clarity, the deconvoluted components are omitted here, and the reader is asked to follow the lower binding energy shoulder of the spectrum, which is predominantly contributed by ZrN in the overall spectral envelope. The stability of this shoulder can be used as a marker of the chemical stability of ZrN NPs. Strong attenuation of the ZrN shoulder can be observed after air annealing at 200 °C and further at higher temperatures. Our previous study on the thermal stability of HfN NPs in air also showed chemical and structural changes that appeared beyond 250 °C, where the HfN NPs tended to become oxidized.[25]

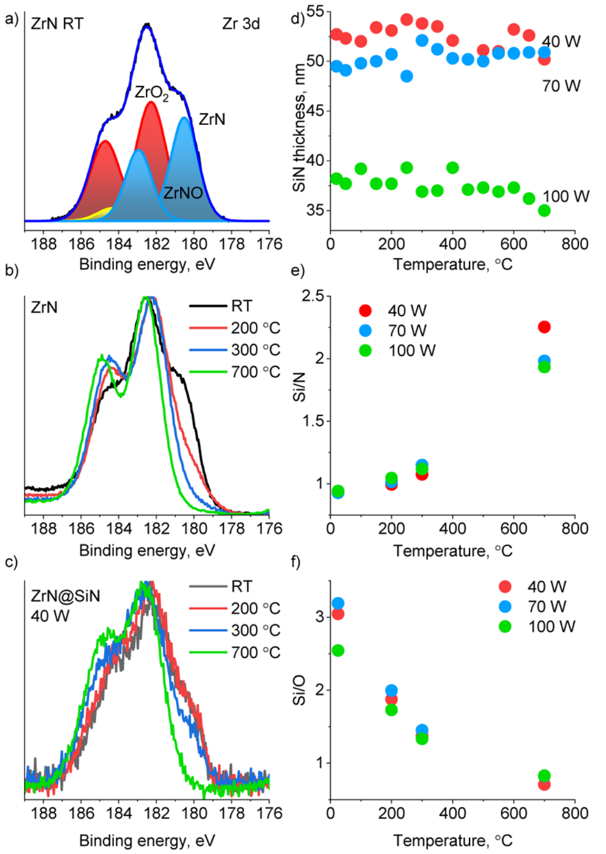

Figure 9. (a) high-resolution XPS Zr 3d peak of ZrN NPs with fitting components; (b,c) evolution of XPS Zr 3d peak of ZrN NPs and ZrN@SiN (40 W) NPs measured ex situ after annealing in air; (d) thickness of SiN films on Si substrates after annealing in air; (e,f) XPS elemental ratios Si/N and Si/O of SiN films on Si substrates after annealing in air.

The formation of the SiN shell over ZrN NPs is, once again, shown to help to shift the oxidation temperature to higher values. Figure 9c shows the Zr 3d XPS spectrum of the ZrN@SiN (40 W) NPs before and after air annealing at different temperatures. The first thing to note is that the signal-to-noise ratio of this spectrum is worse than that of bare ZrN NPs. The effect is given by the low intensity of the XPS signal from the ZrN core, which is strongly screened by the SiN shell. Nevertheless, the quality of the spectral envelope is still sufficient to distinguish the low binding energy of the ZrN shoulder. This is not the case of 70 and 100 W ZrN@SiN NPs (not shown here) that exhibited trace signals of Zr, preventing us from drawing definitive conclusions but supporting our earlier assumption that the SiN shell is thicker at higher rf powers. For ZrN@SiN (40 W) NPs, the XPS analysis does not reveal any significant differences between RT and air annealing at 200 °C, indicating good resistance to oxidation at this temperature. Although slightly attenuated, the ZrN shoulder can still be clearly discerned even at 300 °C, which is also an indication of the higher thermal stability of these NPs compared to bare ZrN NPs. Above 300 °C, the ZrN core of the ZrN@SiN (40 W) NPs becomes heavily oxidized.

The chemical changes in the ZrN core are also accompanied by the chemical transformations associated with the SiN shell. Because the signals from N and O come both from the ZrN core and the SiN shell, it is impossible to discriminate between them using the XPS spectra of ZrN@SiN NPs. As a compromise, we prepared similar SiN films on Si substrates, and Figure 9d−f analyze the thickness and chemical composition of these films before and after air annealing. While the thickness of the films remains constant upon annealing, their chemical composition changes: the SiN films become depleted with nitrogen and enriched with oxygen. No significant difference can be found between the samples prepared at different powers, so the generic chemical formula changes from Si_3N_3O at RT to $SiN_{0.5}O_{1.25}$ for all the samples after annealing at 700 °C. We hypothesize that a similar trend holds for SiN shells created on ZrN NPs, even though the absolute numbers may differ. Hence, SiN can serve as a protective layer for ZrN, but only in the limited temperature range, beyond which the system transforms into core@shell bioxide NPs slightly doped with nitrogen.

4. CONCLUSIONS

ZrN@SiN NPs can be produced in one step using magnetron sputtering-based techniques. To this end, we constructed a combination of a reactive sputter-based gas aggregation cluster source for the production of ZrN NPs and an auxiliary modification chamber for in-flight coating these NPs with an rf-sputtered SiN shell.

The dc sputtering of Zr in the reactive mode using the Ar/N_2 mixture leads to the synthesis of stoichiometric ZrN NPs in the gas phase. Bare ZrN NPs are of a cubic shape, have a mean size of 15 nm, and demonstrate plasmonic properties. They are prone to postdeposition oxidation in air, which results in the formation of the oxynitride layer on the surface and leads to the LSPR position at 850 nm in the near-IR range.

Fluxes of ZrN NPs prepared in the aggregation chamber can be directed by the gas flow to the modification chamber for their in-flight modification via the auxiliary rf magnetron sputtering of Si_3N_4. By carefully tuning the gas pressure and flow in the modification chamber, it is possible to control the residence time of ZrN NPs in front of the Si_3N_4 magnetrons. However, even under the best conditions, this time is in the fraction of a second, which is too short to account for the experimentally measured 5−15 nm thickness of the SiN shell. It is assumed that the capturing of negatively charged ZrN NPs in the electric field of the rf discharge is responsible for a much longer residence time, and rough estimations give a time scale of minutes for such capturing.

The porosity of the in-flight deposited SiN shell can be tuned in the range of 5−30 vol. % by rf power delivered to the Si_3N_4 magnetron, with higher power leading to denser coatings. As a consequence, the effective refractive index of SiN can be adjusted in the range of $n_{630\ \mathrm{nm}} = 1.53{-}1.73$, even though the chemical composition of the shell remains the same. Another effect of the deposition of the SiN shell is related to the fact that ZrN NPs become better protected from oxidation, with denser SiN coatings providing better protection. Overall, the LSPR position of the ZrN@SiN NPs can be tuned from 580 to 850 nm by tuning the density and optical properties of SiN.

The presence of the SiN shell also has a negative effect on the optical performance of the ZrN@SiN NPs: the near-field of the plasmonic ZrN core can hardly spread beyond the thick SiN coating that can make these NPs insensitive for plasmonic sensing. Nevertheless, the porous structure of the SiN shell allows for penetration of the analyte media closer to the ZrN/SiN interface, where the near-field of ZrN can still be effective. In the worst-case scenario of the dense SiN coating, the plasmonic sensitivity of 24 nm/RIU was obtained. This value is far lower than the sensitivity of ideal ZrN and Au NPs, but we consider it still acceptable, especially in high-temperature applications where bare ZrN and Au NPs may fail. As a trade-off, the SiN shell provides a barrier against high-temperature oxidation of ZrN, which results in enhanced thermal stability of the plasmonic response. ZrN@SiN NPs with LSPR position and intensity stable up to 400 °C in air were successfully produced. Furthermore, the NPs with the densest SiN coating demonstrated LSPR up to 700 °C, yet with diminishing intensity.

In summary, this work presents a new route toward the synthesis of core−shell ZrN@SiN NPs with tunable plasmonic properties and enhanced thermal stability in air for use in plasmonic applications at high temperatures. Not least, the newly developed protocol is compatible with microelectronic technologies, avoids the use of harsh chemicals, high temperatures, and is almost waste-free; hence, it minimizes the ecological footprint.

■ ASSOCIATED CONTENT

Supporting Information

The Supporting Information is available free of charge at https://pubs.acs.org/doi/10.1021/acsanm.4c06843.

> Experimental procedure of S_3N_4 target precleaning; details of CFD calculations, including the evaluation of drag force acting on NPs; XPS chemical composition of ZrN/SiN coatings before and after heating in air; size distributiond of ZrN NPs and ZrN@SiN NPs; measurement of S_3N_4 thin film density; optical transmission, reflection, and absorptance of reference quartz substrates; calculated optical extinction, scattering, and absorption spectra of stoichiometric and oxidized ZrN NPs; optical transmittance of ZrN NPs and ZrN@SiN NPs measured in situ during annealing in air; SEM and TEM images of ZrN and ZrN@SiN (100 W) NPs on Si before and after annealing in air at 700 °C (PDF)

■ AUTHOR INFORMATION

Corresponding Authors

Mariia Protsak − *Department of Macromolecular Physics, Faculty of Mathematics and Physics, Charles University, Prague 180 00, Czech Republic;* orcid.org/0000-0001-6942-0095; Email: mariia.protsak@mff.cuni.cz

Andrei Choukourov − *Department of Macromolecular Physics, Faculty of Mathematics and Physics, Charles University, Prague 180 00, Czech Republic;* orcid.org/0000-0002-0582-5453; Email: choukourov@kmf.troja.mff.cuni.cz

Authors

Veronika Červenková − *Department of Macromolecular Physics, Faculty of Mathematics and Physics, Charles University, Prague 180 00, Czech Republic; Department of*

Engineering Physics, Polytechnique Montréal, Montreal, Québec H3T 1J4, Canada
Daniil Nikitin − *Department of Macromolecular Physics, Faculty of Mathematics and Physics, Charles University, Prague 180 00, Czech Republic;* orcid.org/0000-0001-7293-0272
Suren Ali-Ogly − *Department of Macromolecular Physics, Faculty of Mathematics and Physics, Charles University, Prague 180 00, Czech Republic*
Zdenek Krtous − *Department of Macromolecular Physics, Faculty of Mathematics and Physics, Charles University, Prague 180 00, Czech Republic; Department of Engineering Physics, Polytechnique Montréal, Montreal, Québec H3T 1J4, Canada*
Kateryna Biliak − *Department of Macromolecular Physics, Faculty of Mathematics and Physics, Charles University, Prague 180 00, Czech Republic*
Pavel Pleskunov − *Department of Macromolecular Physics, Faculty of Mathematics and Physics, Charles University, Prague 180 00, Czech Republic*
Marco Tosca − *Department of Macromolecular Physics, Faculty of Mathematics and Physics, Charles University, Prague 180 00, Czech Republic; ELI Beamlines Facility, the Extreme Light Infrastructure ERIC, 252 41 Dolní Břežany, Czech Republic*
Ronaldo Katuta − *Department of Macromolecular Physics, Faculty of Mathematics and Physics, Charles University, Prague 180 00, Czech Republic;* orcid.org/0009-0003-8840-7402
Hynek Biederman − *Department of Macromolecular Physics, Faculty of Mathematics and Physics, Charles University, Prague 180 00, Czech Republic*
Bill Baloukas − *Department of Engineering Physics, Polytechnique Montréal, Montreal, Québec H3T 1J4, Canada;* orcid.org/0000-0001-7263-0114
Ludvik Martinu − *Department of Engineering Physics, Polytechnique Montréal, Montreal, Québec H3T 1J4, Canada*
Lucia Bajtosova − *Department of Physics of Materials, Faculty of Mathematics and Physics, Charles University, Prague 121 16, Czech Republic*
Miroslav Cieslar − *Department of Physics of Materials, Faculty of Mathematics and Physics, Charles University, Prague 121 16, Czech Republic*
Milan Dopita − *Department of Condensed Matter Physics, Faculty of Mathematics and Physics, Charles University, Prague 121 16, Czech Republic*

Complete contact information is available at:
https://pubs.acs.org/10.1021/acsanm.4c06843

Notes

The authors declare no competing financial interest.

■ ACKNOWLEDGMENTS

The work was supported by the Czech Science Foundation through the grant GACR 23−06925S. Mariia Protsak acknowledges the support from the Charles University via the student grant GAUK 372322.

■ ADDITIONAL NOTE

[a]Here and further on, for simplicity, the sputtered material will be designated as SiN, even though the real chemical composition is more complex.

■ REFERENCES

(1) Guler, U.; Boltasseva, A.; Shalaev, V. M. Refractory Plasmonics. *Science* **2014**, *344* (6181), 263−264.

(2) Vital, C. V. P.; Farooq, S.; de Araujo, R. E.; Rativa, D.; Gómez-Malagón, L. A. Numerical Assessment of Transition Metal Nitrides Nanofluids for Improved Performance of Direct Absorption Solar Collectors. *Appl. Therm. Eng.* **2021**, *190*, 116799.

(3) Zhang, J.; Wang, C.; Shi, J.; Wei, D.; Zhao, H.; Ma, C. Solar Selective Absorber for Emerging Sustainable Applications. *Adv. Energy Sustainability Res.* **2022**, *3* (3), 2100195.

(4) Wang, X.; Wang, X.; Yue, Q.; Xu, H.; Zhong, X.; Sun, L.; Li, G.; Gong, Y.; Yang, N.; Wang, Z.; Liu, Z.; Cheng, L. Liquid Exfoliation of TiN Nanodots as Novel Sonosensitizers for Photothermal-Enhanced Sonodynamic Therapy against Cancer. *Nano Today* **2021**, *39*, 101170.

(5) Pastukhov, A. I.; Savinov, M. S.; Zelepukin, I. V.; Babkova, J. S.; Tikhonowski, G. V.; Popov, A. A.; Klimentov, S. M.; Devi, A.; Patra, A.; Zavestovskaya, I. N.; Deyev, S. M.; Kabashin, A. V. Laser-Synthesized Plasmonic HfN-Based Nanoparticles as a Novel Multi-functional Agent for Photothermal Therapy. *Nanoscale* **2024**, *16* (38), 17893−17907.

(6) Guler, U.; Shalaev, V. M.; Boltasseva, A. Nanoparticle Plasmonics: Going Practical with Transition Metal Nitrides. *Mater. Today* **2015**, *18* (4), 227−237.

(7) Li, J.; Lou, Z.; Li, B. Nanostructured Materials with Localized Surface Plasmon Resonance for Photocatalysis. *Chin. Chem. Lett.* **2022**, *33* (3), 1154−1168.

(8) Guler, U.; Naik, G. V.; Boltasseva, A.; Shalaev, V. M.; Kildishev, A. V. Performance Analysis of Nitride Alternative Plasmonic Materials for Localized Surface Plasmon Applications. *Appl. Phys. B:Lasers Opt.* **2012**, *107* (2), 285−291.

(9) Barton, D.; Shard, A. G.; Short, R. D.; Bradley, J. W. The Effect of Positive Ion Energy on Plasma Polymerization: A Comparison between Acrylic and Propionic Acids. *J. Phys. Chem. B* **2005**, *109* (8), 3207−3211.

(10) Reinholdt, A.; Detemple, R.; Stepanov, A. L.; Weirich, T. E.; Kreibig, U. Novel Nanoparticle Matter: ZrN-Nanoparticles. *Appl. Phys. B:Lasers Opt.* **2003**, *77* (6−7), 681−686.

(11) Asnaz, O. H.; Drewes, J.; Elis, M.; Strunskus, T.; Greiner, F.; Polonskyi, O.; Faupel, F.; Kienle, L.; Vahl, A.; Benedikt, J. A Novel Method for the Synthesis of Core−Shell Nanoparticles for Functional Applications Based on Long-Term Confinement in a Radio Frequency Plasma. *Nanoscale Adv.* **2023**, *5* (4), 1115−1123.

(12) Alvarez Barragan, A.; Ilawe, N. V.; Zhong, L.; Wong, B. M.; Mangolini, L. A Non-Thermal Plasma Route to Plasmonic TiN Nanoparticles. *J. Phys. Chem. C* **2017**, *121* (4), 2316−2322.

(13) Zakutayev, A.; Perkins, C. L. Influence of Protection Layers on Thermal Stability of Nitride Thin Films. *Phys. Status Solidi Rapid Res. Lett.* **2021**, *15* (8), 1−7.

(14) Saladukhin, I. A.; Abadias, G.; Uglov, V. V.; Zlotski, S. V.; Michel, A.; Janse van Vuuren, A. Thermal Stability and Oxidation Resistance of ZrSiN Nanocomposite and ZrN/SiNx Multilayered Coatings: A Comparative Study. *Surf. Coat. Technol.* **2017**, *332*, 428−439.

(15) Saha, B.; Saber, S.; Naik, G. V.; Boltasseva, A.; Stach, E. A.; Kvam, E. P.; Sands, T. D. Development of Epitaxial Al x Sc 1− x N for Artificially Structured Metal/Semiconductor Superlattice Metamaterials. *Phys. Status Solidi B* **2015**, *252* (2), 251−259.

(16) Chaudhuri, K.; Guler, U.; Azzam, S. I.; Reddy, H.; Saha, S.; Marinero, E. E.; Kildishev, A. V.; Shalaev, V. M.; Boltasseva, A. Remote Sensing of High Temperatures with Refractory, Direct-Contact Optical Metacavity. *ACS Photonics* **2020**, *7* (2), 472−479.

(17) Di, Y.; Qin, T. Plasmonic ZrN@TiO2 Core-Shell Nanostructure Enhancing Photovoltaic Performance of Dye-Sensitized Solar Cells. *Opt. Mater.* **2022**, *132*, 112813.

(18) Exarhos, S.; Alvarez-Barragan, A.; Aytan, E.; Balandin, A. A.; Mangolini, L. Plasmonic Core−Shell Zirconium Nitride−Silicon Oxynitride Nanoparticles. *ACS Energy Lett.* **2018**, *3* (10), 2349−2356.

(19) Berrospe Rodriguez, C.; Alvarez Barragan, A.; Nava, G.; Exarhos, S.; Mangolini, L. Stabilizing the Plasmonic Response of

Titanium Nitride Nanocrystals with a Silicon Oxynitride Shell: Implications for Refractory Optical Materials. *ACS Appl. Nano Mater.* **2020**, *3* (5), 4504−4511.

(20) Dergez, D.; Schneider, M.; Bittner, A.; Schmid, U. Mechanical and Electrical Properties of DC Magnetron Sputter Deposited Amorphous Silicon Nitride Thin Films. *Thin Solid Films* **2015**, *589*, 227−232.

(21) Chaudhuri, K.; Shaltout, A.; Shah, D.; Guler, U.; Dutta, A.; Shalaev, V. M.; Boltasseva, A. Photonic Spin Hall Effect in Robust Phase Gradient Metasurfaces Utilizing Transition Metal Nitrides. *ACS Photonics* **2019**, *6* (1), 99−106.

(22) Biliak, K.; Protsak, M.; Pleskunov, P.; Nikitin, D.; Hanuš, J.; Ali-Ogly, S.; Šomvársky, J.; Tosca, M.; Cieslar, M.; Košutová, T.; Dopita, M.; Lopes Ferreira, F.; Choukourov, A. Plasmonic TiN, ZrN, and HfN Nanofluids for Solar-to-Heat Conversion. *ACS Appl. Nano Mater.* **2023**, *6* (23), 21642−21651.

(23) Protsak, M.; Biliak, K.; Nikitin, D.; Pleskunov, P.; Tosca, M.; Ali-Ogly, S.; Hanuš, J.; Hanyková, L.; Červenková, V.; Sergievskaya, A.; Konstantinidis, S.; Cornil, D.; Cornil, J.; Cieslar, M.; Košutová, T.; Popelář, T.; Ondič, L.; Choukourov, A. One-Step Synthesis of Photoluminescent Nanofluids by Direct Loading of Reactively Sputtered Cubic ZrN Nanoparticles into Organic Liquids. *Nanoscale* **2024**, *16* (5), 2452−2465.

(24) Pleskunov, P.; Košutová, T.; Vaidulych, M.; Nikitin, D.; Krtouš, Z.; Ali-Ogly, S.; Kishenina, K.; Tafiichuk, R.; Biederman, H.; Gordeev, I.; Drewes, J.; Barg, I.; Faupel, F.; Cieslar, M.; Yatskiv, R.; Pihosh, Y.; Nandal, V.; Seki, K.; Domen, K.; Choukourov, A. The Sputter-Based Synthesis of Tantalum Oxynitride Nanoparticles with Architecture and Bandgap Controlled by Design. *Appl. Surf. Sci.* **2021**, *559*, 149974.

(25) Pleskunov, P.; Protsak, M.; Krtouš, Z.; Košutová, T.; Tosca, M.; Biliak, K.; Červenková, V.; Nikitin, D.; Hanuš, J.; Cieslar, M.; Gordeev, I.; Dopita, M.; Vorochta, M.; Kousal, J.; Martinu, L.; Choukourov, A. Refractory Plasmonics of Reactively Sputtered Hafnium Nitride Nanoparticles: Pushing Limits. *Adv. Opt. Mater.* **2024**, *12* (13), 2302715.

(26) Haberland, H.; Karrais, M.; Mall, M. A New Type of Cluster and Cluster Ion Source. *Z. Phys. D: At., Mol. Clusters* **1991**, *20* (1−4), 413−415.

(27) Barke, I.; Hartmann, H.; Rupp, D.; Flückiger, L.; Sauppe, M.; Adolph, M.; Schorb, S.; Bostedt, C.; Treusch, R.; Peltz, C.; Bartling, S.; Fennel, T.; Meiwes-Broer, K.-H.; Moeller, T. The 3D-Architecture of Individual Free Silver Nanoparticles Captured by X-Ray Scattering. *Nat. Commun.* **2015**, *6*, 6187.

(28) Kousal, J.; Shelemin, A.; Schwartzkopf, M.; Polonskyi, O.; Hanuš, J.; Solař, P.; Vaidulych, M.; Nikitin, D.; Pleskunov, P.; Krtouš, Z.; Strunskus, T.; Faupel, F.; Roth, S. V.; Biederman, H.; Choukourov, A. Magnetron-Sputtered Copper Nanoparticles: Lost in Gas Aggregation and Found by in Situ X-Ray Scattering. *Nanoscale* **2018**, *10* (38), 18275−18281.

(29) Shelemin, A.; Pleskunov, P.; Kousal, J.; Drewes, J.; Hanuš, J.; Ali-Ogly, S.; Nikitin, D.; Solař, P.; Kratochvíl, J.; Vaidulych, M.; Schwartzkopf, M.; Kylián, O.; Polonskyi, O.; Strunskus, T.; Faupel, F.; Roth, S. V.; Biederman, H.; Choukourov, A. Nucleation and Growth of Magnetron-Sputtered Ag Nanoparticles as Witnessed by Time-Resolved Small Angle X-Ray Scattering. *Part. Part. Syst. Charact.* **2020**, *37* (2), 1900436.

(30) Pihosh, Y.; Biederman, H.; Slavinska, D.; Kousal, J.; Choukourov, A.; Trchova, M.; Mackova, A.; Boldyreva, A. Composite SiO/Hydrocarbon Plasma Polymer Films Prepared by RF Magnetron Sputtering of SiO2 and Polyethylene or Polypropylene. *Vacuum* **2006**, *81* (1), 32−37.

(31) Drabik, M.; Kousal, J.; Pihosh, Y.; Choukourov, A.; Biederman, H.; Slavinska, D.; Mackova, A.; Boldyreva, A.; Pesicka, J. Composite SiOx/Hydrocarbon Plasma Polymer Films Prepared by RF Magnetron Sputtering of SiO2 and Polyimide. *Vacuum* **2007**, *81* (7), 920−927.

(32) Choukourov, A.; Solar, P.; Polonskyi, O.; Hanus, J.; Drabik, M.; Kylian, O.; Pavlova, E.; Slavinska, D.; Biederman, H. Structured Ti/Hydrocarbon Plasma Polymer Nanocomposites Produced By Magnetron Sputtering with Glancing Angle Deposition. *Plasma Processes Polym.* **2010**, *7* (1), 25−32.

(33) Matěj, Z.; Kužel, R.; Nichtová, L. XRD Total Pattern Fitting Applied to Study of Microstructure of TiO 2 Films. *Powder Diffr.* **2010**, *25* (2), 125−131.

(34) Ali-Ogly, S.; Kousal, J.; Nikitin, D.; Pleskunov, P.; Hanuš, J.; Choukourov, A.; Biederman, H. Computational Fluid Dynamics Predicts the Nanoparticle Transport in Gas Aggregation Cluster Sources. *J. Phys. D Appl. Phys.* **2022**, *55* (44), 445203.

(35) https://saviot.cnrs.fr/miecoat/index.en.html. Accessed October 18, 2024.

(36) Kim, J. H.; Chung, K. W. Microstructure and Properties of Silicon Nitride Thin Films Deposited by Reactive Bias Magnetron Sputtering. *J. Appl. Phys.* **1998**, *83* (11), 5831−5839.

(37) Wang, Y.; Qu, H.; Wang, Y.; Dong, F.; Chen, Z.; Zheng, W. Radio Frequency Plasma-Enhanced Reactive Magnetron Sputtering Deposition of α-SiN x on Photonic Crystal—Laser Diodes for Facet Passivation. *ACS Omega* **2019**, *4* (23), 20205−20211.

(38) Bouhadiche, A.; Difellah, Z.; Bouridah, H.; Remmouche, R.; Benghorieb, S.; Beghoul, M. R.; Benzeghda, S. Modeling and Control of SiNx Film Growth Using the Kinetic Monte Carlo Method: Impact of Gas Flow Rate on Surface Roughness and Film Thickness. *Silicon* **2023**, *15* (12), 5209−5220.

(39) *Handbook of Chemistry and Physics*; Rumble, J., Ed.; Crc Pr Inc, 2024.

(40) Karaballi, R. A.; Humagain, G.; Fleischman, B. R. A.; Dasog, M. Synthesis of Plasmonic Group-4 Nitride Nanocrystals by Solid-State Metathesis. *Angew. Chem.* **2019**, *131* (10), 3179−3182.

(41) Krekeler, T.; Rout, S. S.; Krishnamurthy, G. V.; Störmer, M.; Arya, M.; Ganguly, A.; Sutherland, D. S.; Bozhevolnyi, S. I.; Ritter, M.; Pedersen, K.; Petrov, A. Y.; Eich, M.; Chirumamilla, M. Unprecedented Thermal Stability of Plasmonic Titanium Nitride Films up to 1400 °C. *Adv. Opt. Mater.* **2021**, *9* (16), 2100323.

(42) Setoura, K.; Ito, S. Quantifying the Durability of Transition Metal Nitrides in Thermoplasmonics at the Single-Nanoparticle Level. *AIP Adv.* **2021**, *11* (11), 115027.

(43) Diroll, B. T.; Brumberg, A.; Leonard, A. A.; Panuganti, S.; Watkins, N. E.; Cuthriell, S. A.; Harvey, S. M.; Kinigstein, E. D.; Yu, J.; Zhang, X.; Kanatzidis, M. G.; Wasielewski, M. R.; Chen, L. X.; Schaller, R. D. Photothermal Behaviour of Titanium Nitride Nanoparticles Evaluated by Transient X-Ray Diffraction. *Nanoscale* **2021**, *13* (4), 2658−2664.

(44) Noguchi, S.; Lama, M.; Fujii, Y.; Miura, A.; Tadanaga, K. Structural Color Materials with Color Mixing Effect Using Noble Metal-Free Plasmonic Particles in SiO2−ZrN System. *Adv. Opt. Mater.* **2024**, *12*, 1−9.